
Conformation Clustering of Long MD Protein Dynamics with an Adversarial Autoencoder

Yunlong Liu

Department of Biophysics and Biophysical Chemistry
The Johns Hopkins University
Baltimore, MD 21205
yliu120@jhmi.edu

L. Mario Amzel

Department of Biophysics and Biophysical Chemistry
The Johns Hopkins University
Baltimore, MD 21205
mamzel@jhmi.edu

Abstract

Recent developments in specialized computer hardware have greatly accelerated atomic level Molecular Dynamics (MD) simulations. A single GPU-attached cluster is capable of producing microsecond-length trajectories in reasonable amounts of time. Multiple protein states and a large number of microstates associated with folding and with the function of the protein can be observed as conformations sampled in the trajectories. Clustering those conformations, however, is needed for identifying protein states, evaluating transition rates and understanding protein behavior. In this paper, we propose a novel data-driven generative conformation clustering method based on the adversarial autoencoder (AAE) and provide the associated software implementation **Cong**. The method was tested using a 208 μ s MD simulation of the fast-folding peptide Trp-Cage (20 residues) obtained from the D.E. Shaw Research Group. The proposed clustering algorithm identifies many of the salient features of the folding process by grouping a large number of conformations that share common features not easily identifiable in the trajectory.

1 Introduction

With the development over the past decade of high performance CPU clusters, GPU accelerated computing and software-level optimization, the performance of general molecular dynamics (MD) software (NAMD[20], GROMACS[2], AMBER[22], CHARMM[5], etc.) has been extraordinarily enhanced. Increasingly, individual research groups are capable of running microsecond-scale MD simulations for macromolecular systems of considerable size. Some research laboratories equipped with specialized hardware or large-scale distributed software [23][12] can even produce millisecond-scale trajectories. Considering an MD trajectory as a number of conformations sampled from the complete ensemble (NVE, NVT or NPT) as it is observed through its time evolution, long trajectories provide significant explorations of the conformational space and can reveal key conformational transitions of the macromolecules. Depending on the simulation, those conformational states may reflect stages in the folding of the protein or details about the mechanism of action of the molecules. Objective unbiased identification of these states is crucial for extracting mechanistic information from MD simulations.

Source code of **Cong** is available at <https://github.com/AmzelLab/fiesta3/cong>

Though in some long MD trajectories conformational changes may sometimes be visually recognized, identifying key conformations, grouping similar conformations and quantifying key conformational transitions are more objectively dealt with using specialized software. This is because the number of frames in long trajectories is very large and the dimensionality of the simulation system is high. However, grouping conformations and identifying transitions are often essential for understanding the behavior of the molecules and for comparing changes of their behavior under different environments or those that result from mutations. To tackle these tasks, similarity-based clustering algorithms, such as KMeans, KMedoids, hierarchical clustering, agglomerative clustering and other domain-specific algorithms are used. Their implementations are available as utilities in most major MD packages[2][18][19]. All these similarity-based algorithms share the following common basis: clustering procedures depend on frame-wise similarities, usually quantified by the RMSD. Except for KMeans and KMedoids, which are optimized by expectation maximization, all the other algorithms additionally rely on a pre-determined cutoff to make decisions about how to assign individual frames to a cluster.

Similarity-based clustering algorithms solve the clustering task successfully but a few caveats remain. As MD trajectories are getting longer, the number of frames, denoted by N , is growing by orders of magnitude. Since the computation and space complexity of the RMSD matrix are both $O(N^2)$, algorithms based on calculating the RMSD matrix take large amounts of computing time and can overwhelm the memory. In practice, many researchers run clustering using every n -th frame of the long trajectory; however, this strategy could introduce significant bias into calculations such as those of transition probabilities between clusters. In addition, since RMSDs are essentially Euclidean distances defined on a high dimensional space, clustering using this metric could be vulnerable to artifacts due to their sensitivity to large variations in the conformations of the termini and of flexible loops[3][26]. Some domain-specific RMSD-based clustering methods may suffer from additional side-effects. For instance, the GROMOS algorithm[6] always concatenates two segments of the time series after extracting a neighborhood as a new cluster, which results in a cutoff-sensitive segmentation of the original trajectory. Given these caveats, it is clear that an ideal clustering method should have the following properties: 1) the time and space complexity should be proportional to N ; 2) since defining an ideal distance metric for measuring similarity between structures is very difficult, the algorithm should be data-driven rather than relying on a pre-defined metric. In other words, ideally, the algorithm would "learn" the metric by optimizing some loss function. 3) The algorithm should always look at the entire dataset to avoid unnecessary segmentations.

Recently, deep neural network (dNN) models have been proven to be very successful in the field of Artificial Intelligence (AI). dNN models are powerful in developing very complicated non-linear functions that can map a set of raw image pixels in the data space to some separable regions in the feature space and work conversely as generative models when the probabilistic distributions of the latent representations are available. The training process is entirely data-driven and converges after feeding the entire dataset for a limited number of times ("epochs"). Although dNN models are primarily employed in AI, they are intrinsically general and can be applied to problems in other fields. In this paper, we exploit the data-driven property of dNN, to propose a novel method for clustering MD trajectories based on an existing dNN model – Adversarial Autoencoder (AAE)[16].

2 Theory

2.1 Deep Autoencoder

Deep autoencoders (DAE) are widely used for unsupervised learning tasks such as learning deep representations or dimensionality reduction. Typically, a traditional deep autoencoder consists of two components, the encoder and the decoder. Each component is constructed with a feed-forward neural network, which, in essence, represents a non-linear function. Let's denote the encoder's function as $f_\theta : \mathcal{X} \rightarrow \mathcal{H}$, and denote the decoder's function as $g_\omega : \mathcal{H} \rightarrow \mathcal{X}$, where θ, ω are parameter sets for each function, \mathcal{X} represents the data space and \mathcal{H} the feature (latent) space. The autoencoder used in the model presented here is always aiming at mapping the high-dimensional data space to a lower-dimension feature space and the quality of the mapping is monitored by how well it reconstructs

the original data space from the feature space. For this purpose, it optimizes the reconstruction loss, which is

$$L(\theta, \omega) = \frac{1}{N} \|X - g_\omega(f_\theta(X))\|^2 \quad (1)$$

where $L(\theta, \omega)$ represents the loss function for the reconstruction.

The use of the L^2 -norm in the reconstruction loss is valid for guiding the reconstructions to remain close to the original data. This approach may be contrasted with the L^2 -norm used to measure similarities between frames. In fact, for a finite dimensional vector space V , all l_p norms ($p \geq 1$) are equivalent and induce the same topology. Assuming the dimensionality reduction with DAE is successful, the deep representations generated will feature the major skeleton of MD frames. Therefore, discriminating frames by their deep representations is inherently insensitive to the random noise. Moreover, if we assume a given distribution for the deep representations, the reconstruction function g_ω naturally serves as a generating function that converts the model into a generative model.

2.2 Generative Adversarial Network

Generative Adversarial Network (GAN)[7] is designed to be a deep generative model. It assumes that all observed data are generated from some latent random variable \mathbf{z} with a known prior distribution $p(\mathbf{z})$. The overall goal of GAN is to learn how to generate \mathbf{x} from \mathbf{z} , e.g. finding $p(\mathbf{x}|\mathbf{z})$. A GAN model has two components: a generator network (denoted by function $G(\mathbf{z}; \theta_g)$) and a discriminator network (denoted by function $D(\mathbf{x}; \theta_d)$), which are non-linear functions constructed with multilayer networks. Unlike the autoencoder and many traditional models, GAN is a two-player game rather than an optimizer of a monolithic loss function. The discriminator tries its best to differentiate the real data samples from the generated fake samples, while the generator tries to fool the discriminator by generating counterfeits. When the discriminator is unable to distinguish the source of the input samples, the generator is considered trained. In order to achieve this goal, GAN trains the discriminator and the generator simultaneously in two phases:

$$\min_G \max_D L(D, G) = \mathbb{E}_{\mathbf{x} \sim \mathbb{P}_{data}(\mathbf{x})} [f(D(\mathbf{x}))] + \mathbb{E}_{\mathbf{z} \sim \mathbb{P}_{\mathbf{z}}(\mathbf{z})} [f(1 - D(G(\mathbf{z})))] \quad (2)$$

where $f : \mathbb{R} \rightarrow \mathbb{R}$ and $\mathbb{E}[\cdot]$ denotes the expectation of a random variable.

Standard GAN chooses f as the logarithmic function and the above adversarial loss function adopts the form of the *Jensen-Shannon* (JS) divergence. Training GAN with the JS divergence loss is very likely to fall into unstable traps such as mode collapse. A recently proposed variant of GAN, Wasserstein GAN (WGAN)[4], replaces the JS divergence loss with Wasserstein loss, which is,

$$W(\mathbb{P}_{data}, \mathbb{P}_{G(\mathbf{z})}) = \sup_{\|D\|_L \leq K} \mathbb{E}_{\mathbf{x} \sim \mathbb{P}_{data}} [D(\mathbf{x})] - \mathbb{E}_{\mathbf{x} \sim \mathbb{P}_{G(\mathbf{z})}} [D(\mathbf{x})] \quad (3)$$

Essentially, WGAN substitutes f in Equation 2 with an identity function and this removes the sigmoid activation function in the last layer of the discriminator network. Empirically, WGAN proved to be more stable but it has to be trained with a fairly small step and weight clipping to keep the discriminator function $D(x)$ approximating a K -Lipschitz function. A recent study[8] shows that weight clipping leads to optimization difficulties and could result in pathological behaviors. Instead of tuning an optimal clipping threshold, the study [8] suggests enforcing the Lipschitz constraint by adding a gradient penalty term to the original loss function given by Equation 3. In our experiments, we train both WGAN components in our model with the gradient penalty (Term $\lambda \mathbb{E}_{\hat{\mathbf{x}} \sim \mathbb{P}_{\hat{\mathbf{x}}}} [(\|\nabla_{\hat{\mathbf{x}}} D(\hat{\mathbf{x}})\|_2 - 1)^2]$ in Equation 4), rather than using weight clipping:

$$L(\mathbf{x}) = \mathbb{E}_{\mathbf{z} \sim \mathbb{P}(\mathbf{z})} [D(G(\mathbf{z}))] - \mathbb{E}_{\mathbf{x} \sim \mathbb{P}_{data}} [D(\mathbf{x})] + \lambda \mathbb{E}_{\hat{\mathbf{x}} \sim \mathbb{P}_{\hat{\mathbf{x}}}} [(\|\nabla_{\hat{\mathbf{x}}} D(\hat{\mathbf{x}})\|_2 - 1)^2] \quad (4)$$

where $\hat{\mathbf{x}} = \epsilon \mathbf{x} + (1 - \epsilon)G(\mathbf{z})$, and $\epsilon \sim U[0, 1]$.

2.3 Adversarial Autoencoder

Generally, AAEs have different architectures targeted at different tasks. Since our goal is to use it as a generative clustering method, we adopt the unsupervised version of AAE [16]. This version of the

architecture (see Figure 1) is built based on the data generative process it assumes: each data element \mathbf{x} in the dataset is generated from a latent categorical random variable $\mathbf{y} \sim \text{Cat}(\boldsymbol{\pi})$, represented as a K -dimensional one-hot vector (K is the dimension of \mathbf{y} as well as a user-defined cluster number) and a Gaussian style variable $\mathbf{z} \sim N(0, I)$. The autoencoder component of the AAE estimates the encoding function $p(\mathbf{y}, \mathbf{z}|\mathbf{x})$ and the decoding function $p(\mathbf{x}|\mathbf{y}, \mathbf{z})$ by minimizing the reconstruction loss. Here we denote the encoding function and decoding function as $p(\cdot)$, since in general, $p(\cdot)$ could be modeled as either deterministic functions or probabilistic densities. However, in this paper [16], we model these functions as deterministic. Following the original paper, we denote the estimate of $p(\cdot)$ as $q(\cdot)$. While optimizing the reconstruction loss, the category GAN and the style GAN regulate the autoencoder’s encoder by imposing the prior distribution of \mathbf{y} and \mathbf{z} onto $q(\mathbf{y})$ and $q(\mathbf{z})$, where $q(\cdot)$ is defined as,

$$q(\cdot) = \int_X q(\cdot|x)\mathbb{P}(\mathbf{x})d\mathbf{x} \quad (5)$$

With these considerations, we can write the reconstruction loss as,

$$L = \mathbb{E}_{\mathbf{x} \sim \mathbb{P}(\mathbf{x})} \mathbb{E}_{\substack{\mathbf{y} \sim q_{cat}(\mathbf{y}) \\ \mathbf{z} \sim q_{style}(\mathbf{z})}} \|g_s(g_{cat}(\mathbf{y}) + g_{style}(\mathbf{z})) - \mathbf{x}\|^2 \quad (6)$$

where g_s , g_{cat} and g_{style} denote the decoding function of the shared decoder, the categorical decoder and the style decoder, respectively.

Intuitively, the autoencoder guards the quality of the latent features with its reconstruction loss. The category GAN pushes the categorical feature vector to K -simplex and the style GAN leads $p(\mathbf{z})$ to a standard Gaussian. In other words, AAE assigns an expected $N\pi_i$ number of frames into the i th bucket and each bucket has a standard Gaussian shape. Based on the fact that AAE can impose prior distributions to latent representations successfully, it can feed samples from the prior distributions to the trained generative decoder to create new conformations that do not exist in the original trajectories.

A serious drawback of this method is that it needs to have a correct expectation of the categorical mass π , which is usually impossible to estimate in practice. Intuitively, imposing an incorrect prior knowledge onto the categorical encodings may harm the reconstruction loss, and therefore the quality of the clustering. It remains hard to mathematically estimate the penalty caused by the incorrect prior due to the complex nature of the optimization of this model. A "work-around" solution to this issue is to define a large number of small clusters and assign a uniform distribution to them. This solution can remove the potential penalty to some extent. However, additional analytical steps are needed for further grouping the resulting small clusters and, specifically in MD cases, for understanding the estimated transition probability matrix.

Our proposal is the reparameterization of the categorical prior with a Gumbel-Softmax distribution [14][10] to eliminate the need to specify the categorical mass beforehand. In other words, we propose a special AAE model for clustering that does not need any prior knowledge of how examples are distributed among clusters.

2.4 Adversarial Autoencoder with Gumbel-Softmax

2.4.1 Reparameterization Trick

Reparameterization Trick refers to a sampling process in the machine learning and statistics world. The major aim of using the reparameterization trick is to separate the stochastic sampling part and parameter-dependent transformation part of a parameterized distribution. In stricter terms, it assumes that there is a parameterized distribution $D(\alpha)$, where α is the parameter. To reparameterize $D(\alpha)$, we first sample from an unparameterized distribution Z and then apply a deterministic function that depends on the parameter $f_\alpha(\mathbf{z})$ to the samples to make them as directly sampled from $D(\alpha)$.

After uncoupling the parameters from the stochastic sampling, the distribution parameters become trainable model parameters since their gradients can be estimated by calculating the partial deriva-

tive of the loss function with respect to them. In our case, we rewrite the reconstruction loss by reparameterizing the categorical prior,

$$L = \mathbb{E}_{\mathbf{x} \sim \mathbb{P}(\mathbf{x})} \mathbb{E}_{\substack{\boldsymbol{\alpha} \sim q_{cat}(\boldsymbol{\alpha}) \\ \mathbf{z} \sim q_{style}(\mathbf{z})}} f(h(\boldsymbol{\alpha}, \boldsymbol{\pi}), \mathbf{z}) \quad (7)$$

where $f(\mathbf{y}, \mathbf{z}) = \|g_s(g_{cat}(\mathbf{y}) + g_{style}(\mathbf{z})) - \mathbf{x}\|^2$ and we use $h(\boldsymbol{\alpha}, \boldsymbol{\pi})$ to substitute \mathbf{y} . In addition, we use $\boldsymbol{\alpha}$ to represent a random vector with a fixed distribution and $\boldsymbol{\pi}$ to represent the categorical mass. The function $h(\cdot)$ is the transformation function.

Based on Equation 7, we can obtain the gradient with respect to $\boldsymbol{\pi}$,

$$\nabla_{\boldsymbol{\pi}} L = \mathbb{E}_{\mathbf{x} \sim \mathbb{P}(\mathbf{x})} \mathbb{E}_{\substack{\boldsymbol{\alpha} \sim q_{cat}(\boldsymbol{\alpha}) \\ \mathbf{z} \sim q_{style}(\mathbf{z})}} \nabla_{\boldsymbol{\alpha}} f(h(\boldsymbol{\alpha}, \boldsymbol{\pi}), \mathbf{z}) \nabla_{\boldsymbol{\pi}} h(\boldsymbol{\alpha}, \boldsymbol{\pi}) \quad (8)$$

The *Gumbel-Max Trick*[9][15] is a reparameterization of a one-hot categorical distribution. It samples a d -dimensional vector from a standard Gumbel distribution $\boldsymbol{\alpha}$ and uses $f(\boldsymbol{\alpha}) = \text{onehot}(\text{argmax}(\boldsymbol{\alpha} + \log \boldsymbol{\pi}))$ as the transformation function. Since the argmax function is not a differentiable function, the gradient cannot propagate to the parameter $\boldsymbol{\pi}$. The Gumbel-Softmax distribution aims to relax the Gumbel-Max Trick by replacing the argmax function with softmax .

$$y_i = \frac{\exp((\log \pi_i + \alpha_i)/\tau)}{\sum_{j=1}^k \exp((\log \pi_j + \alpha_j)/\tau)} \quad (9)$$

where $\tau \in (0, +\infty)$ is the temperature parameter.

This distribution was originally introduced as Concrete Distribution by Maddison et al.[14] and was successfully used in a related work[10]. The distribution also relieves the constraint that the categorical mass should belong to the $(k-1)$ -dimensional simplex. π_i s are not necessarily normalized, so they can be anywhere on \mathbb{R}_+ . When directly learning the logits of π_i s, no constraint is needed since the logits belong to \mathbb{R} . The extra parameter τ grants the distribution a few interesting properties. These properties are proved in Supplementary Info A.

Proposition 2.1. *Let \mathbf{y} be a random variable sampled from Equation S1, where $\boldsymbol{\pi} \in (0, +\infty)^d$, $\tau \in (0, +\infty)$, then we have,*

- (1) $\forall k, \lim_{\tau \rightarrow +\infty} y_k = \frac{1}{d}$. In fact, $\lim_{\tau \rightarrow +\infty} y_k$ defines a random variable, which degenerates to a constant $\frac{1}{d}$ everywhere in the event space Ω , which is \mathbb{R}^k .
- (2) $\lim_{\tau \rightarrow 0^+} \mathbf{y} \sim \text{OneHotCategorical}(\frac{\boldsymbol{\pi}}{\sum_{i=1}^k \pi_i})$
- (3) $\tau \rightarrow 0^+, \mathbb{E}y_i = \frac{\pi_i}{\sum_{j=1}^k \pi_j}$.

2.4.2 AAE with Gumbel-Softmax

A general architecture of our model, namely, AAE with Gumbel-Softmax (AAE-GS), is illustrated in Figure 1. By reparameterizing the categorical prior with the Gumbel-Softmax distribution, we extract the categorical mass as a trainable variable, which enables us to impose only the "stochastic" part of the categorical distribution. In this case, the logits of the categorical mass will be updated each time the autoencoder's loss is updated.

To train the model, instead of assuming a categorical mass, we define an annealing process of the parameter τ in Equation (S1). First, we set τ to a large value to simulate $\tau \rightarrow +\infty$. By proposition 2.1, we know the model will approximately put every example in only one cluster, since the categorical representation for each example is almost same. We then anneal τ to a value close to zero in some finite number of steps so that eventually the model can assign each example a one-hot vector marking the most suitable bucket to put it in.

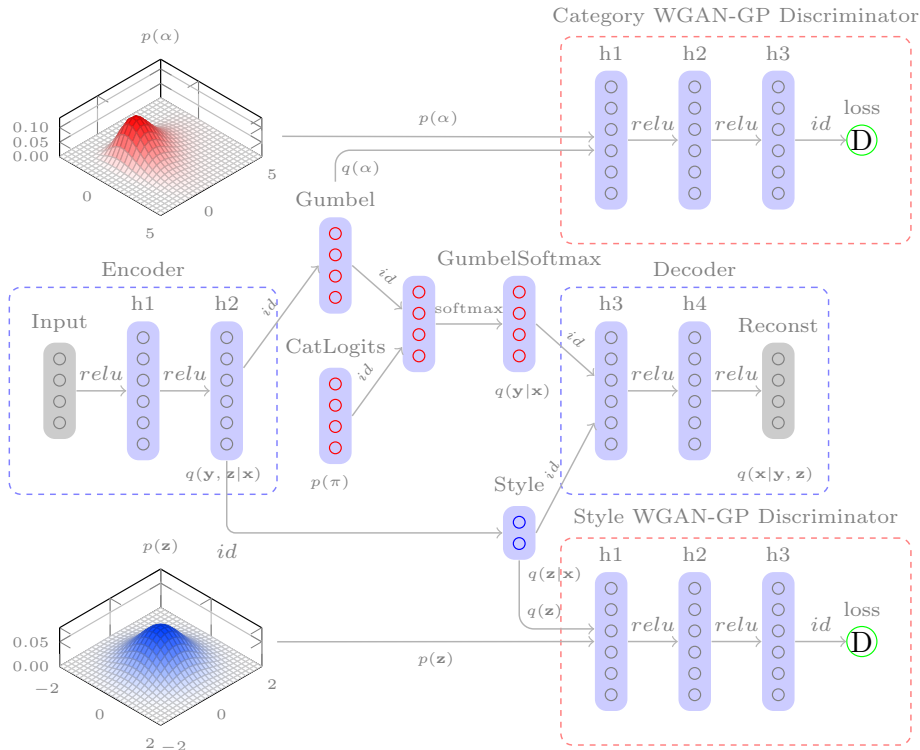


Figure 1: A general architecture of AAE with Gumbel-softmax. The architecture consists of four major components: the encoder, the decoder, the discriminator for categorical GAN and the discriminator for style GAN. Each component is represented as a neural network, which is represented as a multilayer perceptron in this figure. A general choice of activation functions applied to all layers are marked above the arrows connecting all layers. "relu" is short for Rectifier Linear Unit (ReLU) and "id" is short for the identity function. "h1", "h2", etc represent hidden layers in a neural network component. The middle row of the architecture essentially forms a deep autoencoder whose deep representation is divided into a categorical part (red circles) and a style part (blue circles). The encoder combined with the top row forms the categorical GAN and with the bottom row forms the style GAN. $p(\alpha)$ illustrates a Gumbel(0, 1) distribution and $p(z)$ illustrates a standard Gaussian.

3 Results

3.1 Trp-Cage

Unfortunately, a standard dataset for examining the clustering performance of different algorithms for MD frames has not been established yet. To test our algorithms, a model trajectory with the following properties was required: 1) It samples a *small protein*, 2) It is a long enough simulation that traverses a large scope of the protein's conformation space, 3) It samples conformations of the protein that are easily distinguishable by the human eye.

A few years ago, Lindorff-Larsen et al. [13] did a thorough MD based folding study on 12 small proteins with pure MD simulations. It was observed that each protein folded to a conformation very close to its experimentally determined structure during those simulations, and that the process of folding occurred many times during the simulation. There were 9 fast-folding proteins amongst the 12 selected by Lindorff-Larsen et al. We picked a small protein, *Trp-cage* (PDB ID: 2JOF) from these 9 fast-folders. Trp-cage is a 20-residue protein that folds as two small α -helices and a short loop. The fold is stabilized by having a tryptophan residue (Trp6) at the core of the protein with its indole side chain sandwiched between two prolines (Pro12 and Pro18) and surrounded on the other sides by a tyrosine (Tyr3, a leucine (Ieu7) and another proline (Pro19). This protein has a folding time of

14 μs and was simulated for a total of 208 μs . Compared to other fast-folding proteins provided by the study, the folded structure of Trp-cage has clear secondary structure elements that can fold into different conformations even though its length is relatively small. Additionally, its short folding time makes the size of the trajectory compact. For our purposes, this protein is an ideal model for testing the clustering algorithms. The trajectory was generously provided by *D.E. Shaw Research*.

The trajectory we obtained contains a total of 1,044,000 frames assembled in 105 shards. In our clustering experiments, we only considered the backbone coordinates of the protein. Therefore, we sliced each frame by the backbone selection. The selection includes 80 atoms of Trp-Cage so that flattening all the coordinates per frame of these atoms results in a 240-dimensional array. The full trajectory was aligned to a specific frame and translated into TFRecords format specifically designed for Tensorflow[1] Framework and resharded into 10 shards. We used this dataset for all our experiments.

3.2 Clustering with AAE

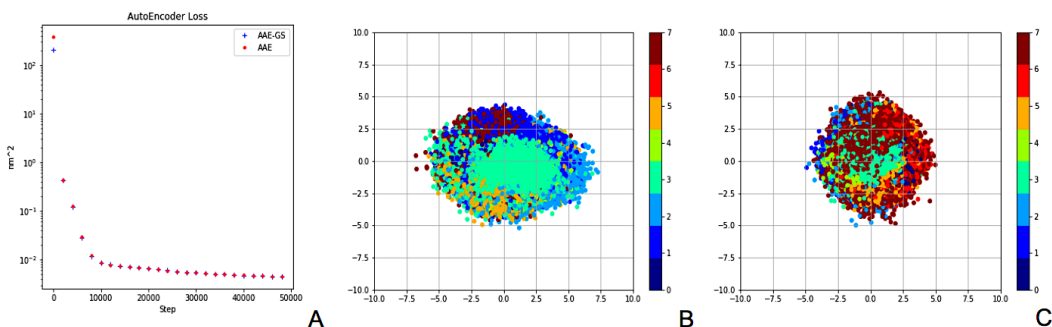


Figure 2: Convergence of AAE and AAE-GS clustering experiments. The reconstruction losses plotted in A of both experiments were evaluated every 2000 steps. B and C plots the first two dimensions of the "learned" style vectors of all frames in AAE and AAE-GS experiments, respectively.

We performed a clustering experiment on our dataset using the general unsupervised architecture of AAE, assuming the categorical prior obeys the discrete uniform distribution and using 8 as the number of clusters. We set the dimension of the style representation to 16 and all its components as independent identically distributed (i.i.d) standard Gaussians. The hyperparameters and the architecture used for this experiment are listed in Table 1 of Supplementary Info B. We trained the model until the autoencoder's loss converged, which took > 24 hours on one NVIDIA Tesla K80 GPU card. (See Figure 2 A). The final reconstruction loss was 0.005 nm^2 , so the average difference between the coordinate of any atom and that in its reconstruction of that atom is approximately 0.7 \AA .

To better visualize frames in each cluster, we sorted the frames in each cluster by the norm of their style vectors from small to large, since we consider that the smaller the norm of the noise the more representative a frame is (Figure 3).

The results show that the uniform categorical prior is successfully imposed on the categorical representation y . The first two dimensions of the style representation for all frames are plotted in Figure 2 B, which shows that the style representation obeys a Gaussian distribution. From the visualization of frames in every cluster, we found that the algorithm identified several featured conformations, for example, cluster 0, 5, 6 and 7 being identified as well-packed conformations, cluster 4 as the unfolded conformation and cluster 3 as some interesting intermediate state on its way to a fully fold conformation. We notice that the frames in cluster 0, 5, and 6 are quite similar and could be treated as duplicate clusters. Intuitively this makes sense, because the folded structure has a greater population among all states since, in the conditions of the simulation, it is energetically stable but we forced every cluster contain the same number of frames.

3.3 Clustering with AAE-GS

Using the same assumption about the distribution of the style vector and its dimension as in the previous experiment, we did a clustering experiment using AAE with Gumbel-Softmax. We use

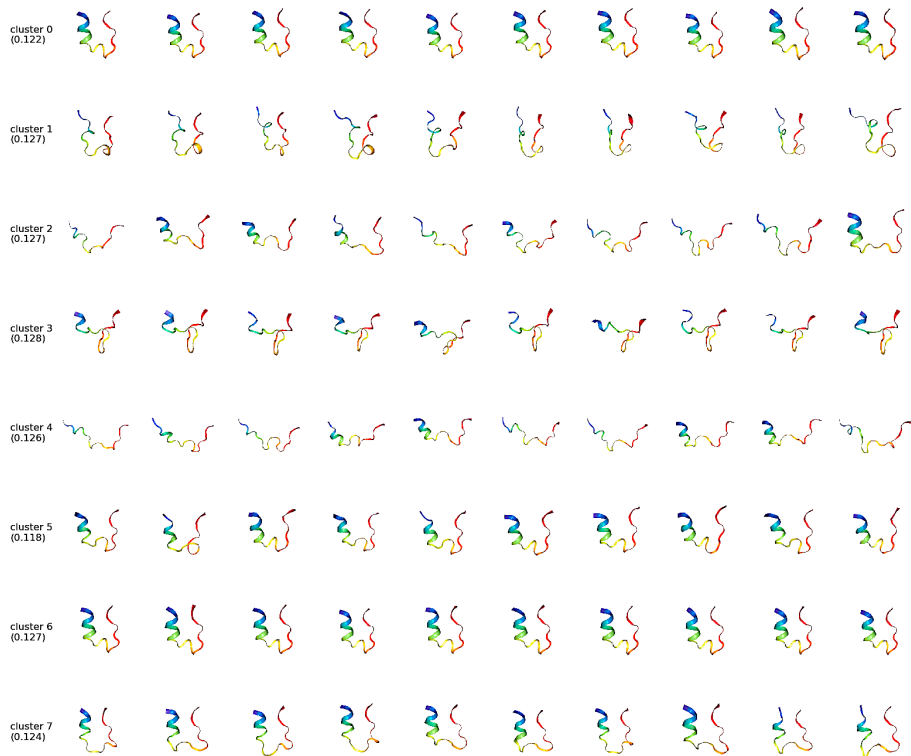


Figure 3: Visualization of cluster representatives obtained from AAE experiment. The first ten frames of each cluster sorted by the norm of the style vector are shown in each row. All structures are oriented to a fixed orientation. The estimated probability mass for each cluster is listed in brackets underneath each cluster id label.

a similar architecture as the previous experiment except that we included the reparametrization with Gumbel-Softmax (See Supplementary Info C). Based on the model of AAE-GS, we define an annealing process of the parameter τ (See Figure 1 in Supplementary Info) to cool down the categorical representation from a uniform vector to a one-hot vector. We trained the model until convergence. AAE-GS takes similar amount of time as the AAE experiment using a similar model architecture. The convergence of the reconstruction loss and the successful imposition of the Gaussian noise are shown in Figure 2 A and C.

This experiment shows that the folded structures are clustered into only one cluster (cluster 3) instead of three duplicated clusters obtained in the AAE experiment. Cluster 3 contains frames with the same characteristics of the folded structure: Trp6 is caged by residues Pro12, Pro18, Tyr3, Leu7 and Pro19. (See Figure 6) The probability mass for this folded cluster is approximately twice the mass of the same cluster in the AAE experiment. It seems that the AAE-GS algorithm tends to aggregate all folded structures within those duplicate clusters into one. However, the probability mass was doubled, not tripled, because the structures in a AAE cluster may not be strictly folded as the norm of the style vector gets larger. The algorithm can categorize those loosely packed structures into other clusters. By comparing all 8 clusters in Figure 4, we found there are no obvious duplicated clusters.

3.4 Generation of fake frames

As explained in the Theory section, with a trained decoding function and latent variables with known distributions, we can generate fake frames that do not exist in the original trajectory. Figure 5 shows a few fake frame examples generated from cluster 4 using the AAE-GS model. The sampled style vector used to generate the fake frame is shown below the structure.



Figure 4: Visualization of cluster representatives obtained from AAE-GS experiment.

The reconstruction quality can be further improved by optimizing the hyperparameters of the model components. For instance, we could add Convolution Neural Networks (CNN) to our model to increase the representation power of all components, which has proven to be very effective in computer vision tasks. Generation of fake frames can enrich the existing dynamics and could be useful for searching for new conformations with specific biophysical relevance.

3.5 An application

To evaluate the significance of the clusters identified in the long Trp-Cage MD trajectory by our AAE-GS computation we assumed that they represent significant intermediates in the folding of the small protein. Several groups have studied the folding of Trp-Cage using MD simulations [24][17][21][25][11]. Some of these studies used clustering and other algorithms to infer a possible folding pathway. In our clustering, it is clear that cluster 0 corresponds to the unfolded state (U) and that cluster 3 corresponds to the fully folded protein (F). The significance of these and the other clusters was explored by using all the clusters as the states of a Markov Model (MM). This computation provided the probabilities of transition between the different states, estimated as

$$p(s_i, s_j) = \frac{c(s_i, s_j)}{\sum_k \sum_l c(s_k, s_l)} \quad (10)$$

where $c(s_i, s_j)$ represents the count of the transitions from state i to state j . It is worth mentioning that $p(s_i, s_j)$ is not a joint probability since i and j are in order. The transition probabilities are defined in such a way that the proportions of each state is reflected.

As seen in Figure 7, some states have only a single probability of transition (besides the return to the same state) while others have transitions to more than one additional state. Based on their

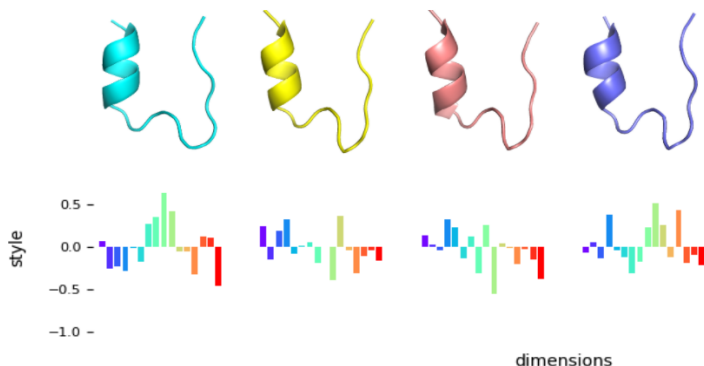


Figure 5: Examples of fake frames generated from the AAE-GS model. The corresponding Gaussian noise vectors are plotted as bar plots. All 16 elements of the style representation are spread out along the horizontal axis of each bar plot. Different dimensions are plotted in different colors.

probabilities of transition the states can be connected in a way that reflects possible pathways from U (state 0) to F (state 3). In this scheme (Figure 7), state 2 is a required intermediate in the folding process. In this state, the helix is starting to form. The two prolines (Pro12 and Pro18) are pointing towards each other and, with Tyr3 they are starting to form the "cage". The tryptophan (Trp6) is still outside the cage but as the helix continues to grow past residue 5, the tryptophan will start to become the center of the cage. It can reach the folded state directly but it can also transition to states 1, 4 or 7. State 1 is a dead-end that has to return to state 2 to reach the folded state 3. State 7 can reach the folded state through two paths: returning to state 2 or transition to state 4 that in turn can reach the folded state 3. State 4 has the largest number of significant transition probabilities: to states 2, 7, 5 and to the folded state (3). It is the last step before reaching the final fold. It has most residues in the correct conformation and would require only an $\sim 100^\circ$ counterclockwise rotation of the helix and small rearrangement to reach the folded state. State 5 is another dead-end. It appears that in state 5, the protein is attempting to fold as an antiparallel hairpin. Since this arrangement does not lead to favorable interactions nor can it evolve into the final fold. It has to return to state 4 to reach the folded state. State 6 is interesting in that it is a not fully-folded conformation that is only accessible from the folded state and may represent a partially unfolded state in equilibrium with the folded state in the conditions of the simulation. This state 4 has a high probability of transition to itself, second only to that of the folded state. The structural descriptions for states mentions above are reflected in Figure 6.

The combination of AAE-GS-identified clusters with a MM using the clusters as the model states, represents an objective analysis of an MD trajectory that provides a highly interpretable model of the folding pathway described by the simulation. The same combination of MD simulations, AAE-GS clustering and MM can be used to identify transitions in enzymes, transporters, channels and others proteins and can become an unbiased procedure to gain insight about the mechanism these proteins.

4 Discussion and Conclusion

Unlike clustering images, clustering MD frames is intrinsically hard since the frame set, which usually comes from trajectories of MD simulation, contains all intermediate conformations of a continuous transformation from one featured state of the macromolecule to another. Clustering such continuous paths is equivalent to determining boundaries at some points of the paths. Consequently, assigning the frames within some neighborhood of the boundaries is somewhat arbitrary. In more formal terms, as our decoder is actually a continuous function, frames with smaller $|z|$ reveal the specific features of a cluster better than those with larger $|z|$. For those frames with large $|z|$, the algorithm is less accurate about their assignment. This indetermination could be resolved by having more clusters, however, more clusters will make features attributed to each cluster less distinguishable. Figures 3, 4 in Supplementary Info plot a random selection of frames from the first 10,000 frames of each cluster with the same clustering results from the AAE and AAE-GS experiments, respectively. We found

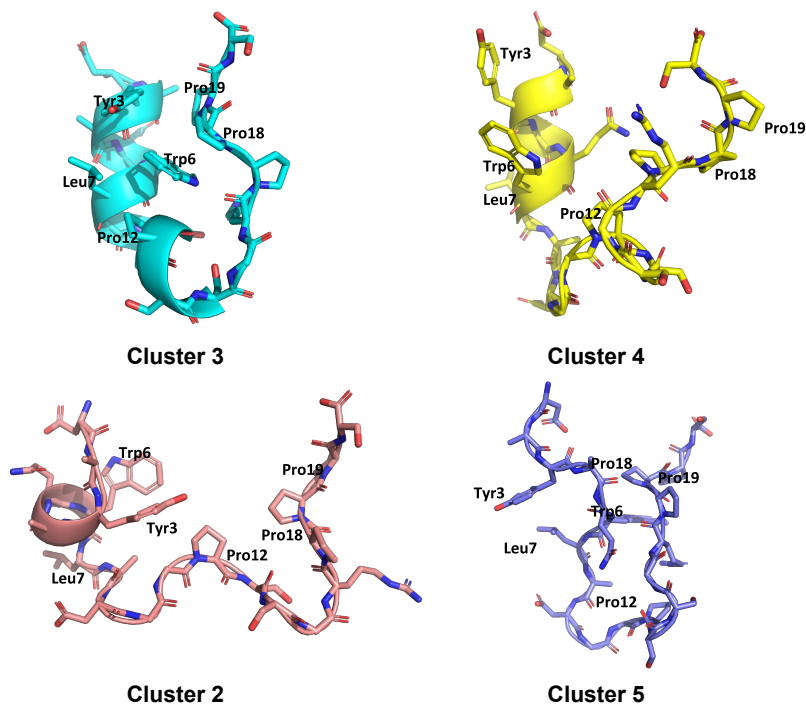


Figure 6: Structural descriptions for selective states. The backbone of the protein is plotted with the representation Cartoon and key residues are shown with balls and sticks.

that the majority of frames in the random selection still preserve specific features that identified their clusters.

From a technical perspective, the general architecture we propose for clustering could be enhanced by involving CNNs and other types of networks. The hyperparameters of all network components are subject to automatic tuning in order to achieve the smallest reconstruction error. Currently, a major caveat of training our model is the lack of robustness of the two GAN components. However, as more and more efforts[4][8] on stabilizing GAN are brought into play in the machine learning community, we expect to have a stable way of training GAN components and tuning the hyperparameters of the discriminators.

We showed that the AAE-GS algorithm we propose is effective in clustering MD accessed conformations and it naturally provides a quantity $|z|$ that represents the loyalty of a frame to the cluster it belongs to. In addition, we showed that our clustering results can be useful in revealing and quantifying important biophysical properties of macromolecules, such as folding landscapes, allosteric rearrangements and transitions among active and inactive conformations.

Acknowledgments

We acknowledge Maryland Advanced Research Computing Center (MARCC) for providing hardware resource and support. We thank D.E. Shaw Research for kindly providing us the 208 μ s trajectory of Trp-Cage.

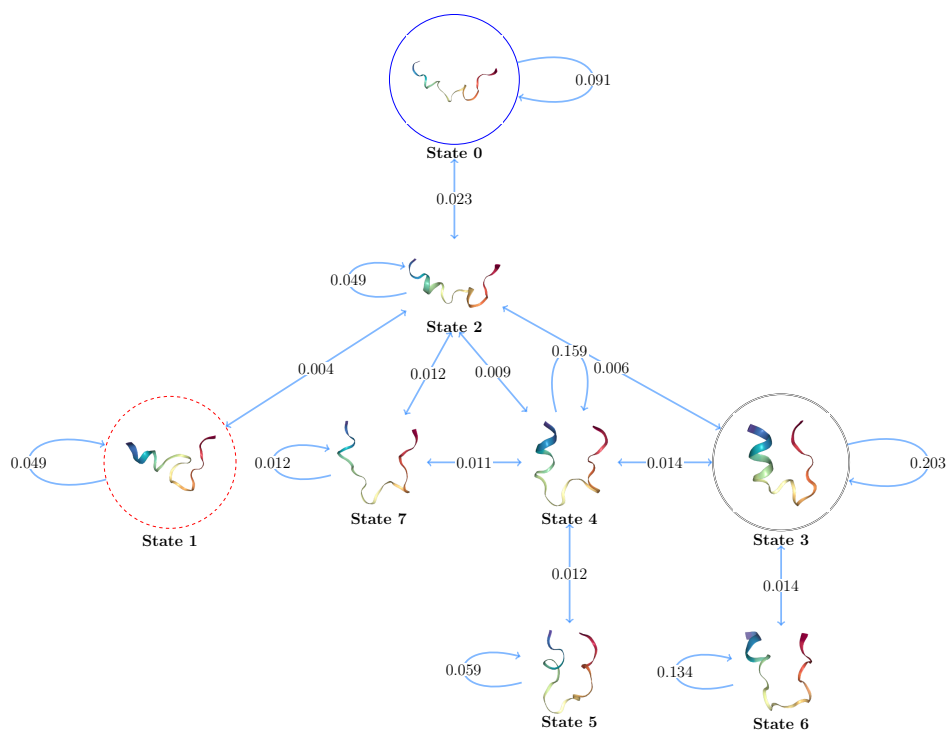


Figure 7: Transitions between different states of Trp-cage. The first frame in each cluster is used as the representation of the cluster. The unfolded state is circled in blue. The perfect folded state is double circled in black. A misfolded state (State 1) is circled in red dashes. All transition probabilities are sit in the middle of the arrow. Arrows with a transition probability lower than 0.005 are pruned.

References

- [1] Martin Abadi, Paul Barham, Jianmin Chen, Zhifeng Chen, Andy Davis, Jeffrey Dean, Matthieu Devin, Sanjay Ghemawat, Geoffrey Irving, Michael Isard, Manjunath Kudlur, Josh Levenberg, Rajat Monga, Sherry Moore, Derek G. Murray, Benoit Steiner, Paul Tucker, Vijay Vasudevan, Pete Warden, Martin Wicke, Yuan Yu, and Xiaoqiang Zheng. Tensorflow: A system for large-scale machine learning. In *12th USENIX Symposium on Operating Systems Design and Implementation (OSDI 16)*, pages 265–283, 2016.
- [2] Mark James Abraham, Teemu Murtola, Roland Schulz, Szilárd Páll, Jeremy C. Smith, Berk Hess, and Erik Lindahl. Gromacs: High performance molecular simulations through multi-level parallelism from laptops to supercomputers. *SoftwareX*, 1–2:19 – 25, 2015.
- [3] Charu C. Aggarwal, Alexander Hinneburg, and Daniel A. Keim. On the surprising behavior of distance metrics in high dimensional space. In *Lecture Notes in Computer Science*, pages 420–434. Springer, 2001.
- [4] Martin Arjovsky, Soumith Chintala, and Léon Bottou. Wasserstein generative adversarial networks. In Doina Precup and Yee Whye Teh, editors, *Proceedings of the 34th International Conference on Machine Learning*, volume 70 of *Proceedings of Machine Learning Research*, pages 214–223, International Convention Centre, Sydney, Australia, 06–11 Aug 2017. PMLR.
- [5] B.R. Brooks, III C.L. Brooks, and Jr. A.D. MacKerell. Charmm: The biomolecular simulation program. *J Comput Chem.*, 30(10):1545–1614, 2009.
- [6] Xavier Daura, Karl Gademann, Bernhard Jaun, Dieter Seebach, Wilfred F van Gunsteren, and Alan E Mark. Peptide folding: when simulation meets experiment. *Angewandte Chemie International Edition*, 38(1-2):236–240, 1999.
- [7] Ian Goodfellow, Jean Pouget-Abadie, Mehdi Mirza, Bing Xu, David Warde-Farley, Sherjil Ozair, Aaron Courville, and Yoshua Bengio. Generative adversarial nets. In Z. Ghahramani, M. Welling, C. Cortes, N. D. Lawrence, and K. Q. Weinberger, editors, *Advances in Neural Information Processing Systems 27*, pages 2672–2680. Curran Associates, Inc., 2014.
- [8] Ishaan Gulrajani, Faruk Ahmed, Martín Arjovsky, Vincent Dumoulin, and Aaron C. Courville. Improved training of wasserstein gans. *CoRR*, abs/1704.00028, 2017.
- [9] E.J. Gumbel. *Statistical theory of extreme values and some practical applications: a series of lectures*. Applied mathematics series. U. S. Govt. Print. Office, 1954.
- [10] Eric Jang, Shixiang Gu, and Ben Poole. Categorical reparameterization with gumbel-softmax. 2017.
- [11] J Juraszek and PG Bolhuis. Sampling the multiple folding mechanisms of trp-cage in explicit solvent. *Proceedings of the National Academy of Sciences*, 103(43):15859–15864, 2006.
- [12] S. M. Larson, C. D. Snow, M. Shirts, and V. S. Pande. Folding@Home and Genome@Home: Using distributed computing to tackle previously intractable problems in computational biology. *ArXiv e-prints*, January 2009.
- [13] K. Lindorff-Larsen, S. Piana, R.O. Dror, and D.E. Shaw. How fast-folding proteins fold. *Science*, Oct 28;334(6055):517-20., 2011.
- [14] Chris J. Maddison, Andriy Mnih, and Yee Whye Teh. The concrete distribution: A continuous relaxation of discrete random variables. *CoRR*, abs/1611.00712, 2016.
- [15] Chris J. Maddison, Daniel Tarlow, and Tom Minka. A* Sampling. In *Advances in Neural Information Processing Systems 27*, 2014.
- [16] Alireza Makhzani, Jonathon Shlens, Navdeep Jaitly, and Ian Goodfellow. Adversarial autoencoders. In *International Conference on Learning Representations*, 2016.
- [17] Fabrizio Marinelli, Fabio Pietrucci, Alessandro Laio, and Stefano Piana. A kinetic model of trp-cage folding from multiple biased molecular dynamics simulations. *PLoS computational biology*, 5(8):e1000452, 2009.
- [18] Robert T. McGibbon, Kyle A. Beauchamp, Matthew P. Harrigan, Christoph Klein, Jason M. Swails, Carlos X. Hernández, Christian R. Schwantes, Lee-Ping Wang, Thomas J. Lane, and Vijay S. Pande. Mdtraj: A modern open library for the analysis of molecular dynamics trajectories. *Biophysical Journal*, 109(8):1528 – 1532, 2015.

- [19] Naveen Michaud-Agrawal, Elizabeth J. Denning, Thomas B. Woolf, and Oliver Beckstein. Mdanalysis: A toolkit for the analysis of molecular dynamics simulations. *Journal of Computational Chemistry*, 32(10):2319–2327, 2011.
- [20] J. C. Phillips, R. Braun, W. Wang, J. Gumbart, E. Tajkhorshid, E. Villa, C. Chipot, R. D. Skeel, L. Kale, and K. Schulten. Scalable molecular dynamics with NAMD. *J Comput Chem*, 26(16):1781–1802, Dec 2005.
- [21] Jed W Pitera and William Swope. Understanding folding and design: Replica-exchange simulations of “trp-cage” miniproteins. *Proceedings of the National Academy of Sciences*, 100(13):7587–7592, 2003.
- [22] R. Salomon-Ferrer, D.A. Case, and R.C. Walker. An overview of the amber biomolecular simulation package. *WIREs Comput. Mol. Sci.*, 3:198–210, 2013.
- [23] D. E. Shaw, J. P. Grossman, J. A. Bank, B. Batson, J. A. Butts, J. C. Chao, M. M. Deneroff, R. O. Dror, A. Even, C. H. Fenton, A. Forte, J. Gagliardo, G. Gill, B. Greskamp, C. R. Ho, D. J. Ierardi, L. Iserovich, J. S. Kuskin, R. H. Larson, T. Layman, L. S. Lee, A. K. Lerer, C. Li, D. Killebrew, K. M. Mackenzie, S. Y. H. Mok, M. A. Moraes, R. Mueller, L. J. Nociolo, J. L. Peticolas, T. Quan, D. Ramot, J. K. Salmon, D. P. Scarpazza, U. B. Schafer, N. Siddique, C. W. Snyder, J. Spengler, P. T. P. Tang, M. Theobald, H. Toma, B. Towles, B. Vitale, S. C. Wang, and C. Young. Anton 2: Raising the bar for performance and programmability in a special-purpose molecular dynamics supercomputer. pages 41–53, Nov 2014.
- [24] Christopher D Snow, Bojan Zagrovic, and Vijay S Pande. The trp cage: folding kinetics and unfolded state topology via molecular dynamics simulations. *Journal of the American Chemical Society*, 124(49):14548–14549, 2002.
- [25] Ruhong Zhou. Trp-cage: folding free energy landscape in explicit water. *Proceedings of the National Academy of Sciences*, 100(23):13280–13285, 2003.
- [26] Arthur Zimek, Erich Schubert, and Hans-Peter Kriegel. A survey on unsupervised outlier detection in high-dimensional numerical data. *Statistical Analysis and Data Mining*, 5(5):363–387, 2012.

Supplemental Info: Conformation Clustering of Long MD Protein Dynamics with an Adversarial Autoencoder

A Proof of Proposition 2.1

Lemma A.1. Let \mathbf{g} be a d -dimensional random vector and all its components are independent identical distributed (i.i.d) random variables with a Gumbel $(0, 1)$ distribution. $\boldsymbol{\pi}$ be a d -dimensional vector in $(0, +\infty)^d$ and τ is an arbitrary number in $R_{>0}$. Let's define a d -dimensional random vector \mathbf{y} by transforming \mathbf{g} with function \mathbf{f} , where $\mathbf{f}: R^d \rightarrow R^d$. The k th element of \mathbf{f} is

$$y_k = f_k(\mathbf{g}) = \frac{\exp((\log(\pi_k) + g_k)/\tau)}{\sum_k \exp((\log(\pi_k) + g_k)/\tau)} \quad (\text{S1})$$

where y_k , g_k and π_k are the k th element of \mathbf{y} , \mathbf{g} and $\boldsymbol{\pi}$, respectively. Then we have, $\forall k' \in \{1, \dots, d\}$,

$$p(y_{k'} = \max_k y_k \mid \boldsymbol{\pi}, \tau) = \frac{\pi_{k'}}{\sum_k \pi_k} \quad (\text{S2})$$

Proof. Let's first consider the conditional probability of $y_{k'} = \max_k y_k$ given $\boldsymbol{\pi}$, τ and $g_{k'} = g$. Since g_k s are i.i.d. and $y_{k'}$ is the maximum among all elements of \mathbf{y} , we have,

$$\begin{aligned} p(y_{k'} = \max_k y_k \mid \boldsymbol{\pi}, \tau, g_{k'} = g) &= \prod_{k \neq k'} p(y_k \leq y_{k'}) \\ &= \prod_{k \neq k'} p(\log \pi_k + g_k \leq \log \pi_{k'} + g) \\ &= \prod_{k \neq k'} p(g_k \leq \frac{\pi_{k'}}{\pi_k} + g) \end{aligned} \quad (\text{S3})$$

Since $g_k \sim \text{Gumbel}(0, 1)$ and the cumulative distribution function of $\text{Gumbel}(0, 1)$ is $e^{-e^{-x}}$, $x \in \mathbb{R}$, we substitute $p(g_k < \frac{\pi_{k'}}{\pi_k} + g)$ with $\exp(-\exp(-\log(\frac{\pi_{k'}}{\pi_k}) - g))$. Then we have,

$$\begin{aligned} p(y_{k'} = \max_k y_k \mid \boldsymbol{\pi}, \tau, g_{k'} = g) &= \prod_{k \neq k'} \exp(-\exp(-\log(\frac{\pi_{k'}}{\pi_k}) - g)) \\ &= \exp \sum_{k \neq k'} (-\exp(-\log(\frac{\pi_{k'}}{\pi_k}) - g)) \\ &= \exp \sum_{k \neq k'} (-\frac{\pi_k}{\pi_{k'}} e^{-g}) \\ &= \exp(-e^{-g} \frac{\sum_{k \neq k'} \pi_k}{\pi_{k'}}) \end{aligned} \quad (\text{S4})$$

The probability density function of $\text{Gumbel}(0, 1)$ is $e^{-x-e^{-x}}$, where $x \in \mathbb{R}$. Marginalize out the $g_{k'}$, we have,

$$\begin{aligned} p(y_{k'} = \max_k y_k \mid \boldsymbol{\pi}, \tau) &= \int_{g_{k'}} p(y_{k'} = \max_k y_k \mid \boldsymbol{\pi}, \tau, g_{k'} = g) p_{g_{k'}}(g) dg \\ &= \int_{-\infty}^{+\infty} \exp(-e^{-g} \frac{\sum_{k \neq k'} \pi_k}{\pi_{k'}}) e^{-g-e^{-g}} dg \\ &= \int_{-\infty}^{+\infty} \exp(-g - e^{-g} \frac{\sum_k \pi_k}{\pi_{k'}}) dg \end{aligned} \quad (\text{S5})$$

Let $C = \frac{\sum_k \pi_k}{\pi_{k'}}$, the improper integral in the last step of Equation S5 can be rewritten as $\int_{-\infty}^{+\infty} \exp(-g - Ce^{-g})dg$.

This integral can be easily calculated by substituting g with $-\log t$. We have,

$$\begin{aligned} \int_{-\infty}^{+\infty} \exp(-g - Ce^{-g})dg &= \int_0^{+\infty} e^{-Ct} dt = \\ &= -\frac{1}{C} e^{-ct} \Big|_0^{+\infty} \\ &= \frac{1}{C} \end{aligned} \quad (\text{S6})$$

Substituting C back to $\frac{\sum_k \pi_k}{\pi_{k'}}$ completes the proof. \square

Proposition A.1. Let \mathbf{y} be a random variable sampled from Equation S1, where $\boldsymbol{\pi} \in (0, +\infty)^d$, $\tau \in (0, +\infty)$, then we have,

- (1) $\forall k, \lim_{\tau \rightarrow +\infty} y_k = \frac{1}{d}$. In fact, $\lim_{\tau \rightarrow +\infty} y_k$ defines a random variable, which degenerates to a constant $\frac{1}{d}$ everywhere in the event space Ω , which is \mathbb{R}^k .
- (2) $\lim_{\tau \rightarrow 0^+} \mathbf{y} \sim \text{OneHotCategorical}(\frac{\boldsymbol{\pi}}{\sum_{i=1}^k \pi_i})$
- (3) $\tau \rightarrow 0^+, \mathbb{E}y_i = \frac{\pi_i}{\sum_{j=1}^k \pi_j}$.

Proof. (1) $\forall \omega \in \Omega, \forall k \in \{1, \dots, d\}, |g_k| < +\infty$, so as $|\log(\pi_k) + g_k| < +\infty$. In this case, when $\tau \rightarrow +\infty, (\log(\pi_k) + g_k)/\tau \rightarrow 0$ and $\exp((\log(\pi_k) + g_k)/\tau) \rightarrow 1$. It is trivial to see $y_k = \frac{1}{d}$.

- (2) Since \mathbf{g} is a random vector defined on the event space \mathbb{R}^d , which is denoted as Ω in the following text, $\mathbf{y} = \mathbf{f} \circ \mathbf{g}$ is also defined on Ω . Let's start by defining a partition of Ω .

Consider a series of subsets of Ω , denoted by $\{A_k\}$ where k is the index. Each A_k is defined as $\{\omega \mid \omega \in \Omega, k \in I_{max}, |I_{max}| = 1\}$, where $I_{max} = \arg \max_k (g_k(\omega) + \log(\pi_k))$ and $|\cdot|$ denotes the cardinality. Let's define another set $A_{>1}$ as $\{\omega \mid \omega \in \Omega, |I_{max}| > 1\}$. Since \mathbf{g} is a d -dimensional random vector, $\forall \omega, |I_{max}| \leq d$. In addition, since $\forall \omega$, each component of $\mathbf{g}(\omega)$ is finite and bounded, then there must be at least one maximum. This implies $|I_{max}| \geq 1, \forall \omega$. Therefore, it is trivial to see $(\cup_k A_k) \cup A_{>1}$ is a partition of Ω .

Let's consider the value of $\lim_{\tau \rightarrow 0^+} y_k$ on each A_k . $\forall \omega \in A_k$, by definition, we have, for $\forall j, j \in \{1, \dots, d\}$,

$$\begin{aligned} y_j = f_j(\mathbf{g}(\omega)) &= \frac{\exp((\log(\pi_j) + g_j)/\tau)}{\sum_i \exp((\log(\pi_i) + g_i)/\tau)} \\ &= \frac{\exp((\log(\pi_j) + g_j - \log(\pi_k) - g_k)/\tau)}{\sum_i \exp((\log(\pi_i) + g_i - \log(\pi_k) - g_k)/\tau)} \end{aligned} \quad (\text{S7})$$

The last step of Equation S7 is obtained by dividing the term $\exp(\log(\pi_k) + g_k)$ from both the numerator and the denominator. It is trivial to see that for any $j \neq k$, $\lim_{\tau \rightarrow 0^+} \exp((\log(\pi_j) + g_j - \log(\pi_k) - g_k)/\tau) = 0$ and only when $j = k$, the limit is equal to 1. This is also true for i in the denominator. Then we can conclude, for any index k ,

$$\forall \omega \in A_k, \lim_{\tau \rightarrow 0^+} y_j = 1 \text{ when } j = k, \text{ otherwise } 0. \quad (\text{S8})$$

Similarly as the above analysis, we can draw the corresponding conclusion for set $A_{>1}$.

$$\forall \omega \in A_{>1}, \lim_{\tau \rightarrow 0^+} y_j = \frac{1}{|I_{max}|} \text{ when } j \in I_{max}, \text{ otherwise } 0. \quad (\text{S9})$$

For simplicity, we use \mathbf{e}_k to denote the unit vector on k -th dimension in \mathbb{R}^d , which is defined as only the k -th element is 1 and all others are 0. And we denote the set that contains all values of $\lim_{\tau \rightarrow 0^+} \mathbf{y}$ in Equation S9 as O . Then Equation S8 implies $p(A_k) \leq p(\lim_{\tau \rightarrow 0^+} \mathbf{y} = \mathbf{e}_k)$ and Equation S9 implies $p(A_{>1}) \leq p(O)$.

It is also trivial to see that $\lim_{\tau \rightarrow 0^+} \mathbf{y}(\omega) = \mathbf{e}_k$ implies $\omega \in A_k$. This can be proved by contradiction. Assume $\omega \notin A_k$, since $(\cup_k A_k) \cup A_{>1}$ is a partition of Ω , ω must be in any other set A_j where $j \neq k$ or $A_{>1}$. Apparently this is impossible because of Equation S8 and S9. Then we have $p(\lim_{\tau \rightarrow 0^+} \mathbf{y} = \mathbf{e}_k) \leq p(A_k)$ and $p(O) \leq p(A_{>1})$.

$$\begin{aligned} p(A_k) &= p(\lim_{\tau \rightarrow 0^+} \mathbf{y} = \mathbf{e}_k) \\ p(A_{>1}) &= p(O) \end{aligned} \quad (\text{S10})$$

Due to Lemma A.1 and its proof, we know $p(A_k) = \frac{\pi_k}{\sum_i \pi_i}$. (Please notice that Gumbel(0, 1) is a continuous distribution, so $p(y_k \leq g_{k'}) = p(y_k < g_{k'})$ in the proof of Lemma A.1.) By summing k , we have $\sum_k p(A_k) = 1$. On the other hand, because of the fact that $(\cup_k A_k) \cup A_{>1}$ is a partition of Ω , $\sum_k p(A_k) + p(A_{>1}) = 1$. Then we get $p(A_{>1}) = 0$, which makes the points in $A_{>1}$ and O unmeaningful. (This can be seen in another way that $A_{>1}$ is exactly a zero-measure set.) It turns out that $\lim_{\tau \rightarrow 0^+} \mathbf{y}$ is defined only on $\{\mathbf{e}_k\}$. Take $\{\mathbf{e}_k\}$ as Ω' and \mathcal{F}' is the σ -algebra on it. Combining with the result in Equation S10, we get the distribution of $\lim_{\tau \rightarrow 0^+} \mathbf{y}$ as,

$$p'(\lim_{\tau \rightarrow 0^+} \mathbf{y} = \mathbf{e}_k) = \frac{\pi_k}{\sum_i \pi_i} \quad (\text{S11})$$

which is usually written as

$$p'(\lim_{\tau \rightarrow 0^+} \mathbf{y}) = \prod_j \left(\frac{\pi_j}{\sum_i \pi_i} \right)^{y_j} \quad (\text{S12})$$

where p' is the probability measure defined on the probability space $(\Omega', \mathcal{F}', p')$.

(3) This is a trivial corollary of (2).

□

B AAE Experiment

In our experiment, the architecture of AAE we used consists of 8 multilayer perceptrons (MLP): 1) The Shared Encoder encoding the raw data to a shared deep representation that could be further decomposed into a categorical id and the noise, 2) The Categorical Encoder mapping the shared representation to an one-hot categorical vector, 3) The Style Encoder translating the shared representation to a gaussian noise, 4) The Categorical Decoder and 5) The Style Decoder reconstructing the shared representation from the categorical id and the noise, 6) The Shared Decode reconstructing the raw data from the shared representation, 7) The Discriminator of Categorical-WGAN and 8) The Discriminator of Style-WGAN. The structure of each components are listed in the following table 1.

¹Since all components are modeled with MLP, we represents the layers of MLP with numbers separate with "×". Each number refers to the number of nodes in that layer.

²Note for the subscript and superscript: "BN" refers to Batch Normalization; "DO" prefixed with a number refers to dropout and the number is the dropout probability; Superscript refers to an activation function other than "relu". We use "relu" as the default activation function.

Table 1: Structures of all sub-components of our AAE model.

Component	Architecture ¹
Shared Encoder	$400_{\text{BN}, 0.1 \text{ DO}} \times 400_{\text{BN}} \times 400_{\text{BN}}^2$
Categorical Encoder	$100_{\text{BN}} \times 8^{\text{softmax}}$
Style Encoder	$200_{\text{BN}} \times 16^{\text{id}}$
Categorical Decoder	$100_{0.1 \text{ DO}} \times 400_{\text{BN}}$
Style Decoder	$200_{0.1 \text{ DO}} \times 400_{\text{BN}}$
Shared Decoder	$400_{\text{BN}, 0.1 \text{ DO}} \times 400_{\text{BN}} \times 240_{\text{BN}}^{\text{id}}$
Discriminator (Cat-GAN)	$400_{0.1 \text{ DO}} \times 400_{0.1 \text{ DO}} \times 400 \times 200 \times 200 \times 200 \times 200 \times 1^{\text{id}}$
Discriminator (Style-GAN)	$400_{0.1 \text{ DO}} \times 400_{0.1 \text{ DO}} \times 400 \times 200 \times 200 \times 200 \times 200 \times 1^{\text{id}}$

We use the Adam Optimizer ($\beta_1 = 0.5, \beta_2 = 0.9$) to optimize all loss functions with a minibatch of 4096 shuffled examples. The learning rate for updating the autoencoder is 2.0×10^{-5} . For both the categorical GAN and the style GAN, we use a learning rate of 2.0×10^{-4} to train and a gradient penalty weight of 10 to regularize the weights.

C AAE with Gumbel Softmax Experiment

We use a very similar model architecture as the AAE Experiment. We simply replace the activation function of the last layer of Categorical Encoder with "id". This is because we need to produce "fake" samples of the Gumbel distributions.

We anneal the parameter τ from 10 to 0.01 in the first 20000 steps with a power 4 of polynomial decay. After 20000 steps, τ was remained as 0.01. The following figure depicts the annealing process of τ .

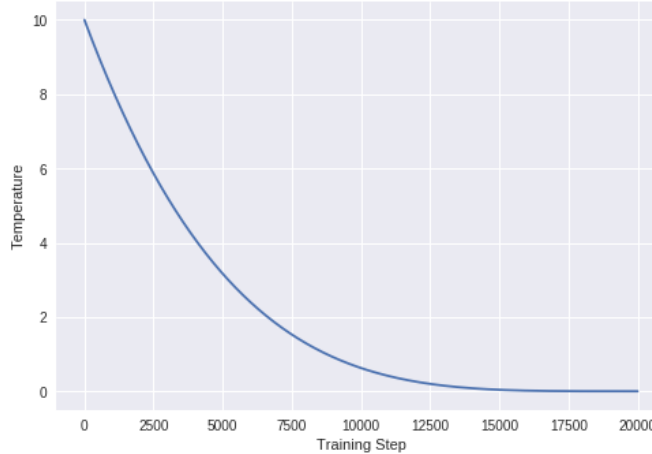


Figure S1: The annealing process of the parameter τ .

D Architecture of AAE

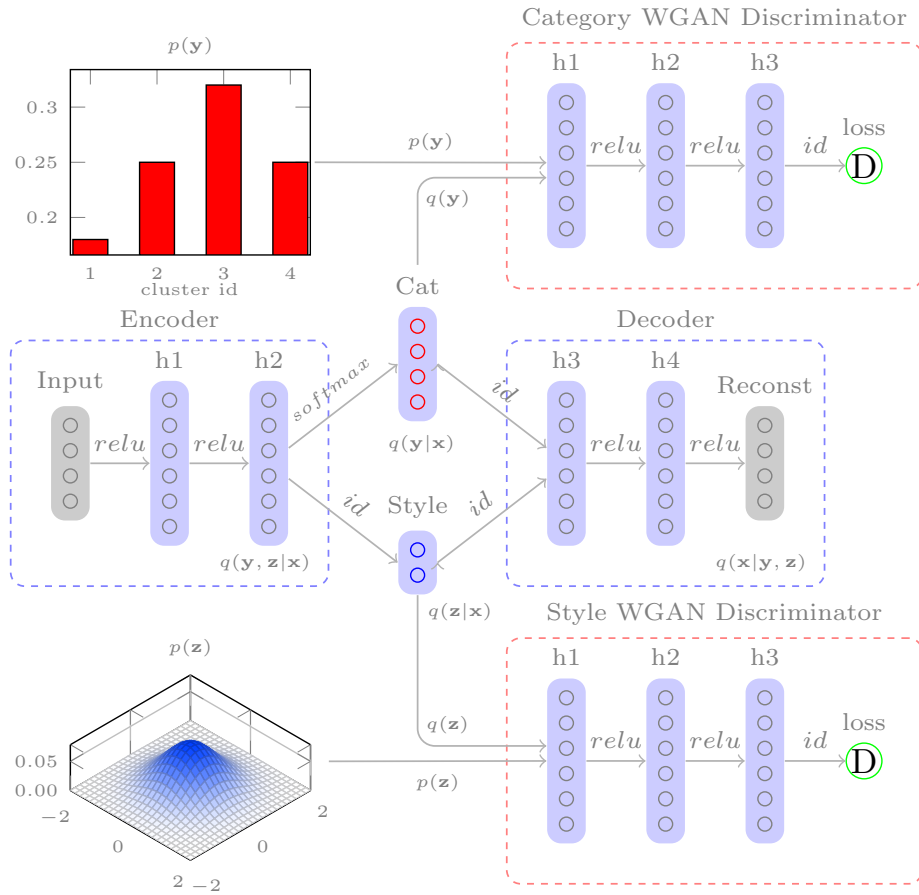


Figure S2: The general architecture of AAE for clustering. This architecture is represented in a similar way as the one of AAE with Gumbel-Softmax.

E Visualization on Random Selections of Clustering Results

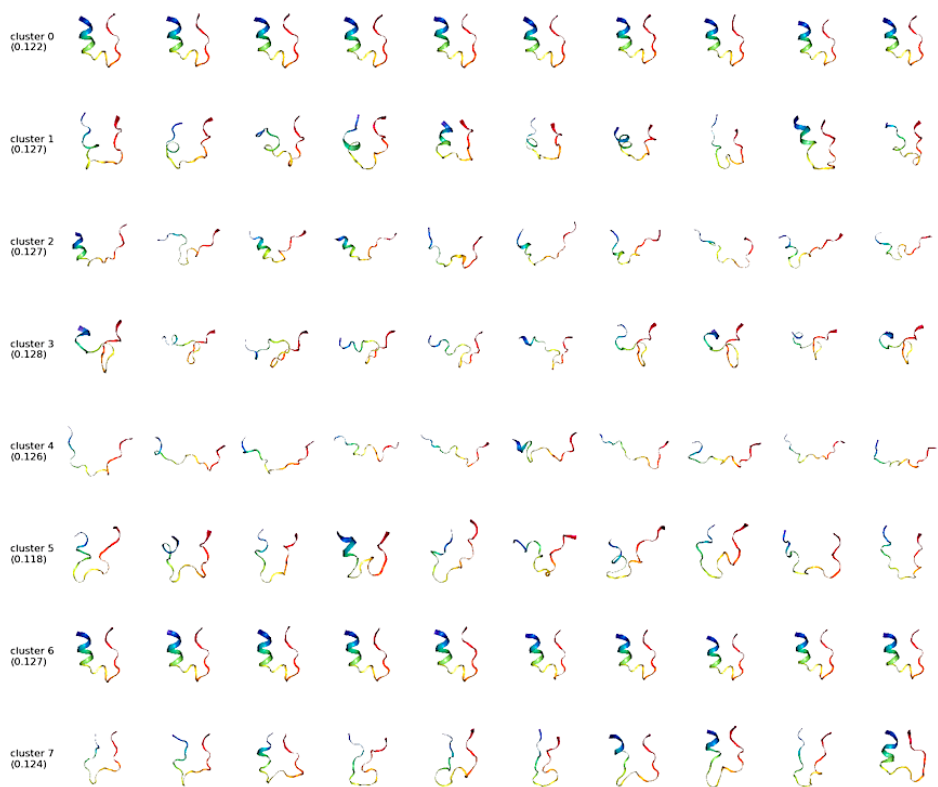


Figure S3: Random frames selected from the first 10,000 of each cluster (AAE)



Figure S4: Random frames selected from the first 10,000 of each cluster (AAE-GS)